

Structural analysis of thin films of novel polynorbornene derivatives by grazing incidence X-ray scattering and specular X-ray reflectivity along with ellipsometry

Taek Joon Lee,^{a‡} Gwang-su Byun,^{a,b‡} Kyeong Sik Jin,^{a‡} Kyuyoung Heo,^{a‡} Gahee Kim,^a Sang Youl Kim,^b Iwhan Cho^{b*} and Moonhor Ree^{a*}

^aDepartment of Chemistry, National Research Lab for Polymer Synthesis and Physics, Pohang Accelerator Laboratory, Center for Integrated Molecular Systems, Polymer Research Institute, and BK School of Molecular Science, Pohang University of Science and Technology (POSTECH), Pohang 790-784, Republic of Korea, and

^bPolyolefin Materials Research Center, Department of Chemistry, and BK21 Program, Korea Advanced Institute of Science and Technology (KAIST), Daejeon 305-701, Republic of Korea.

Correspondence e-mail: icho@kaist.ac.kr, ree@postech.edu

In the present study, structural analyses using synchrotron grazing incidence X-ray scattering, specular reflectivity and ellipsometry were performed on thin films of two novel polynorbornene derivatives, chiral poly(norbornene acid methyl ester) and racemic poly(norbornene acid *n*-butyl ester), which are potential low dielectric constant materials for advanced microelectronic and display applications. These analyses provided important information on the structure, electron density gradient across the film thickness, chain orientation, refractive index and thermal expansion characteristics of the polymers in substrate-supported thin films. The structural characteristics and properties of the thin films depended on the tacticity of the polymer chain and were further influenced by the film thickness and thermal annealing history.

© 2007 International Union of Crystallography
Printed in Singapore – all rights reserved

1. Introduction

Cyclic olefin polymers have attracted attention from academia and industry over the last 15 years because of their excellent properties (high glass transition temperature, high optical transparency, low birefringence, and low moisture absorption) and their potential applications in the flexible flat panel displays and microelectric and microfluidic devices (Angiolini *et al.*, 2003; Bhusari *et al.*, 2001; Byun *et al.*, 2006; Lipian *et al.*, 2002; Shick *et al.*, 1998). A representative cyclic olefin polymer is polynorbornene (Angiolini *et al.*, 2003; Bhusari *et al.*, 2001; Breunig & Risse, 1992; Byun *et al.*, 2006; Grove *et al.*, 1999; Heinz *et al.*, 1998; Lipian *et al.*, 2002; Mathew *et al.*, 1996; Reinmuth *et al.*, 1996; Shick *et al.*, 1998). However, this polymer exhibits very low solubility in common organic solvents and poor processibility, as well as interfacial adhesion failure, making it unsuitable for use in applications such as flexible flat panel displays and microelectric and microfluidic devices. Therefore, much research effort has been devoted to modifying this polymer *via* chemical functionalization and copolymerization so as to improve its solubility, processibility and interfacial adhesion properties (Breunig & Risse, 1992; Byun *et al.*, 2006; Grove *et al.*, 1999; Heinz *et al.*, 1998; Mathew *et al.*, 1996; Reinmuth *et al.*, 1996; Shin *et al.*, 2004). As part of these efforts, a series of poly(norbornene carboxylic acid ester)s with high solubility were developed, and their mechanical, optical and electrical properties were investigated (Breunig & Risse, 1992; Mathew *et al.*, 1996; Reinmuth *et al.*, 1996; Heinz *et al.*, 1998; Grove *et al.*, 1999). Those studies, however, characterized the properties of the polymers

in the bulk rather than in nanometer-scale thin films. If these polymers are to be used in device applications such as those outlined above, quantitative data on their structures and properties in the thin film state are absolutely necessary.

In the present study, we sought to analyze the structure and properties of nanometer-scale thin films of two novel poly(norbornene acid ester) derivatives supported on silicon substrates, using synchrotron grazing incidence X-ray scattering (GIXS) and specular X-ray reflectivity (XR) along with spectroscopic ellipsometry. The novel poly(norbornene acid ester) derivatives, chiral poly(norbornene carboxylic acid methyl ester) (*C*-PNME) and racemic poly(norbornene carboxylic acid *n*-butyl ester) (*R*-PNBE) (Fig. 1), were synthesized according to the method of Byun *et al.* (2006). By analyzing the GIXS, XR and ellipsometry data, we obtained detailed structural parameters as well as information on the orientation and other properties of these polymers in thin films.

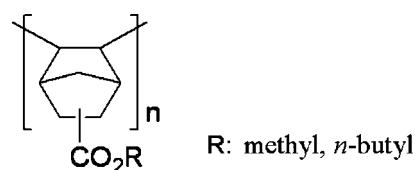


Figure 1
Chemical structures of chiral poly(norbornene carboxylic acid methyl ester) (*C*-PNME) and racemic poly(norbornene carboxylic acid *n*-butyl ester) (*R*-PNBE).

‡ T. J. Lee, G. Byun, K. S. Jin and K. Heo contributed equally to this work.

2. Experiment

2.1. Material and film preparation

C-PNME [highly isotactic (the detailed isotacticity is under investigation); 72000 number-average molecular weight \overline{M}_n and 1.50 polydispersity index (PDI)] and R-PNBE (atactic; 60000 \overline{M}_n and 1.45 PDI) were synthesized according to a previously reported method (Byun *et al.*, 2006). Thermogravimetric analysis indicated that both polymers begin thermal degradation at 648 K in a nitrogen atmosphere. In differential scanning calorimetry (DSC) measurements, the polymers did not show a peak characteristic of crystal melting when heated at 10.0 K min⁻¹ from 203 K to near the degradation temperature 648 K. Moreover, in the DSC analysis, glass transition temperatures (T_g) of the polymers could not be detected, which might be attributed to small changes in their heat of fusion at the glass transition. However, dynamic mechanical thermal analysis found that R-PNBE has *ca* 483 K T_g . The T_g analysis of C-PNME is still in progress.

For each polymer, a series of solutions with concentrations of 0.5–5.0 wt% were prepared in chloroform, and filtered through polytetrafluoroethylene membranes of pore size 0.2 μm . The solutions were spin-coated onto pre-cleaned silicon substrates and dried at 353 K for 15 h under vacuum, followed by cooling to room temperature at a rate of 0.2 K min⁻¹. Some of the dried films were further annealed for an additional 15 h at 423 or 473 K, followed by cooling to room temperature at a rate of 0.2 K min⁻¹. The thicknesses of the obtained films were determined to be in the range 20–450 nm by means of ellipsometry.

2.2. Measurement

GIXS measurements were carried out at the 4 C2 beamline of the Pohang Accelerator Laboratory (PAL) (Bolze *et al.*, 2001; Ree & Ko, 2005; Yu *et al.*, 2005). The sample-to-detector distance was 170 mm, and an X-ray radiation source of wavelength $\lambda = 0.154$ nm and a two-dimensional charge-coupled detector (Roper Scientific, Trenton, NJ, USA) were used. Samples were mounted on a Huber z -axis goniometer equipped with a vacuum chamber. The incidence angle α_i of the X-ray beam was set at 0.20–0.22°, which is between the critical angles of the films and the silicon substrate ($\alpha_{c,f}$ and $\alpha_{c,s}$). Scattering angles were corrected by the positions of X-ray beams reflected from the silicon substrate interface with changing incidence angle α_i and by

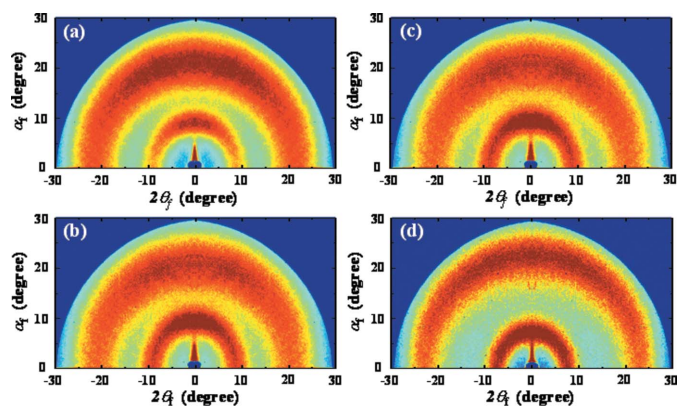


Figure 2
Two-dimensional GIXD patterns measured at $\alpha_i = 0.22^\circ$ for (a) C-PNME film (467 nm thick) as prepared; (b) C-PNME film annealed at 473 K; (c) R-PNBE film (437 nm thick) as prepared; and (d) R-PNBE film annealed at 473 K. α_f and $2\theta_f$ are the exit angles of the scattered X-ray beam with respect to the film surface and to the plane of incidence respectively.

a pre-calibrated silver behenate standard (TCI, Japan). A set of aluminium foil pieces was employed as semi-transparent beam stops because the intensity of the specular reflection from the substrate was much stronger than the intensity of GIXS near the critical angle. Data were typically collected for 30–60 s.

Specular XR data were measured at the 3C2 beamline (Bolze *et al.*, 2002; Park *et al.*, 1995) of the PAL. Samples were mounted on a Huber four-circle goniometer, and a scintillation counter with an enhanced dynamic range (Bede Scientific, EDR) was used as a detector. Measured reflected intensities were normalized to the intensity of the incident beam, which was monitored using an ionization chamber.

Ellipsometric measurements were also performed using spectroscopic ellipsometers (model M-2000 & VASE, Woollam, Lincoln, NE, USA). The VASE ellipsometer was used for quantitative data measurements. In particular, to investigate out-of-plane optical anisotropy, measurements were performed at several incident angles of the probe beam with respect to the film surface (15, 45, and 75°). The M-2000 ellipsometer, which was equipped with a home made hot stage and an Eurotherm temperature controller with a K-type thermocouple, was used to perform *in-situ* measurements as a function of temperature during the heating of the films, according to the following protocol: sample temperature was raised from 303–423 K in increments of 5 K, with a heating rate of 3.0 K min⁻¹ for each step and a soaking time of 5 min at each temperature. Using the same heating protocol, measurements were additionally performed on the same silicon substrates without the polymer film in order to determine the values of the refractive index n and extinction coefficient k as a function of temperature of the silicon substrate used in the film preparation (Oh & Ree, 2004). The thus-obtained temperature-dependent n and k data of the substrate were used in the analysis of the ellipsometry data of the films deposited on the substrates.

3. Results and discussion

Fig. 2 shows the two-dimensional GIXS patterns obtained from C-PNME and R-PNBE polymer films with thicknesses of about 450 nm before and after thermal annealing at 473 K. Similar GIXS patterns were observed for thinner films before and after annealing at 423 K and 473 K (data not shown). For both the C-PNME and R-PNBE films, the scattering patterns show only two broad rings without any Bragg reflections, indicating that the films contained no crystalline

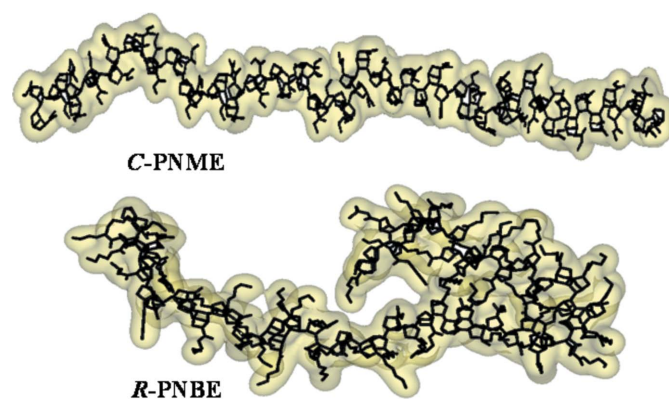


Figure 3
Schematic molecular representations of 64-repeat-unit fragments of (a) C-PNME and (b) R-PNBE polymer chains, obtained by molecular simulation using the *Cerius²* software package (Accelrys, San Diego, CA, USA).

structures. The lack of features indicative of crystalline structures in the scattering patterns is consistent with the DSC results, which showed no evidence of crystal melting. The two broad rings in the scattering patterns are therefore assigned as amorphous halos. The d -spacing values determined from the halos were 12.4 and 5.3 Å for the as-prepared *C*-PNME film [Fig. 2(a)], and 15.0 and 5.1 Å for the as-prepared *R*-PNBE film [Fig. 2(c)]. The d -spacing values for each polymer film were found to be unaffected by annealing at 473 K [Fig. 2(b) and (d)].

To understand the origins of the two halo rings, we sought to determine the most stable chain conformation of each polymer by molecular simulation using the *Cerius*² software package (Accelrys, San Diego, CA, USA); the simulations were performed using a chain of length 64 chemical repeat units. The results are shown in Fig. 3. As can be seen in the figure, the *C*-PNME polymer chain prefers a helical conformation along the longitudinal chain axis. Considering this helical chain conformation, the inter-chain distance of *C*-PNME polymer molecules is estimated to be 12–13 Å, which is comparable to the d -spacing value (12.4 Å) of the first halo ring in the low scattering angle region. The average pitch distance of the side groups along the helical chain axis is determined to be 5–6 Å, which is comparable to the d -spacing value (5.34 Å) of the second halo ring in the high scattering angle region. The optimal conformation of the *R*-PNBE polymer was also found to be a helical chain, but the overall chain shape is somewhat different from that of the *C*-PNME polymer (Fig. 3). As a result, the helical *R*-PNBE polymer chain has an overall molecular shape that is shortened along the helical axis but bulky along the direction normal to that axis. For this shortened and bulky helical chain conformation, the inter-chain distance of *R*-PNBE polymer molecules is estimated to be around 15 Å, which corresponds to the d -spacing value (15.0 Å) of the first halo ring in the low scattering angle region, and the pitch distance of the side groups along the helical chain axis is estimated to be 5 Å, which is close to the d -spacing value (5.1 Å) of the second halo ring in the high scattering angle region. Taking these results into account, we assign the first halo ring to the mean inter-distance of the polymer chains in a helical conformation, and the second halo ring to the mean pitch distance of the side groups in the helical chain.

In the scattering patterns in Fig. 2, the amorphous halo rings are anisotropic, rather than isotropic, along their azimuthal angle in the $\alpha_f - 2\theta_f$ plane, where α_f and $2\theta_f$ are the exit angles of the scattered X-ray beam with respect to the film surface and to the plane of incidence respectively. Furthermore, the anisotropy of the first halo ring is stronger in the *C*-PNME film than in the *R*-PNBE film. Considering these observations, we extracted the one-dimensional scattering profiles of the first halo ring of the polymer films along the azimuthal

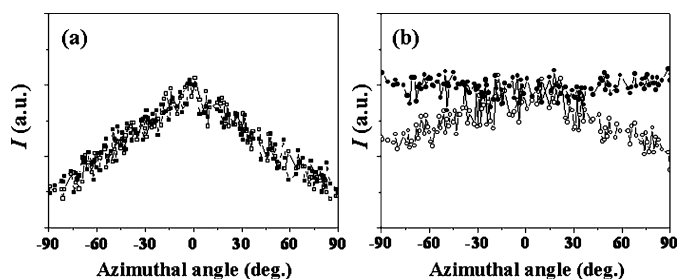


Figure 4 One-dimensional scattering profiles extracted along the azimuthal angle of the first halo ring at the scattering angle where the maximum intensity appeared, obtained from the two-dimensional GIXS patterns in Fig. 2. (a) *C*-PNME film before (open squares) and after annealing at 473 K (filled squares); (b) *R*-PNBE film before (open circles) and after annealing at 473 K (filled circles).

angle line at the scattering angle where the intensity is highest (Fig. 4). The *C*-PNME film [Fig. 4(a)] clearly shows a relatively strong anisotropy of the first halo ring, with the scattering intensity in the out-of-plane direction being stronger than that in the film plane. This anisotropic halo ring was not significantly influenced by annealing at 473 K [Fig. 4(a)]. Given that this halo ring originates from the mean inter-chain distance, as discussed above, the observed anisotropic character indicates that the *C*-PNME polymer chains in the thin film were preferentially oriented along the film plane, rather than randomly.

The *R*-PNBE film [Fig. 4(b)] also exhibits anisotropy in the one-dimensional scattering profile of the first halo ring along the azimuthal angle line; however, annealing at 473 K caused the complete disappearance of this anisotropy. These results indicate that the *R*-PNBE polymer chains are weakly oriented along the film plane in the as-prepared film, but that the weakly developed in-plane chain orientation is destroyed by post annealing.

Considering the morphological and in-plane chain orientation characteristics determined from the analyses described above, we performed XR analysis on the films annealed at 473 K. Representative XR data are displayed in Fig. 5. The 140.6 nm thick *C*-PNME film [Fig. 5(a)] exhibits two critical angles of the film and the substrate ($\alpha_{c,f}$ and $\alpha_{c,s}$) over the q_z range of 0.20–0.33 nm⁻¹; here q_z is the magnitude of the scattering vector along the direction of the film thickness,

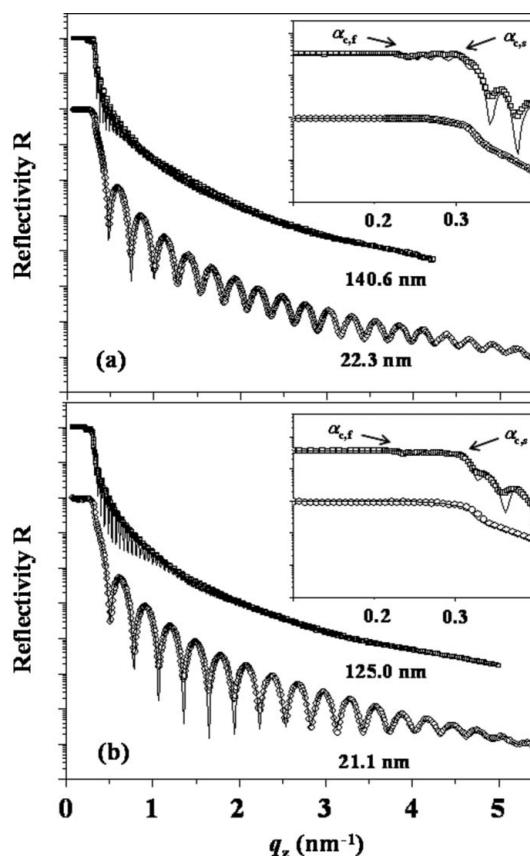


Figure 5 (a) Representative XR profiles of *C*-PNME films (22.3 and 140.6 nm thick), which were annealed at 473 K. (b) Representative XR profiles of *R*-PNBE films (21.1 and 125.0 nm thick), which were annealed at 473 K. The symbols are the measured data and the solid line represents the fit curve assuming a homogeneous electron density distribution within the film except for a thin surface layer, in which the electron density is slightly different. The inset shows a magnification of the region around the two critical angles: $\alpha_{c,f}$ and $\alpha_{c,s}$ are the critical angles of the film and the silicon substrate respectively.

Table 1

Structural parameters of the C-PNME and R-PNBE films annealed at 473 K, obtained by XR measurements and data analysis.

Film	d^\dagger (bulk) (nm)	d^\ddagger (skin) (nm)	σ^\ddagger (nm)	ρ_e (bulk) § (nm ⁻³)	ρ_e (skin) ¶ (nm ⁻³)	$\rho_{e,f}^{\dagger\dagger}$ (nm ⁻³)
C-PNME (1)	21.1	1.2	0.1	357	326	355
C-PNME (2)	138.7	1.9	0.1	398	402	398
R-PNBE (1)	19.6	1.5	0.1	354	299	350
R-PNBE (2)	124.2	0.8	0.1	385	364	385

† Thickness of the bulk and skin layers. ‡ Film surface roughness. § Electron density of the bulk. ¶ Electron density of the skin layer. †† Electron density averaged over the entire film.

which is defined by $q_z = (4\pi/\lambda) \sin \theta$, where λ is the wavelength of the X-ray beam and θ is the grazing incident angle. Oscillations between the two critical angles are also discernible, which are the waveguide modes for X-rays confined in the film. Once θ exceeds the critical angle of the substrate, a significant portion of the beam penetrates into the substrate and the reflected intensity drops sharply. The steeply decaying reflectivity curve is modulated by high frequency oscillations, referred to as Kiessig fringes (Kiessig, 1931). These fringes appear owing to interference between the light reflected from the film–air surface and that reflected from the film–substrate interface. As the angle increases, the XR profile shows an overall decay of the reflected intensity and of the modulation amplitudes, which can be attributed to the presence of the film–substrate interface and to surface roughness. This XR profile was well fitted by the Parratt formalism (Parratt, 1954) with a structural model that assumed a homogeneous electron density distribution throughout the film except for a thin surface layer, in which the electron density is slightly different [Fig. 5(a)]. It is noteworthy, however, that the minima of the Kiessig fringes are considerably shallower in the experimental data than in the theoretical curve. This discrepancy may be associated with several factors, including a slightly inhomogeneous film thickness on the length scale of the projected beam size, curvature of the substrate induced by residual stress at the substrate–film interface, and so on. The analysis of the XR data determined the film structure, surface roughness, thickness, and average film electron density; here, the average film electron density $\rho_{e,f}$ was obtained from the measured $\alpha_{c,f}$ using the relationship $\rho_{e,f} = (\pi\alpha_{c,f}^2)/(r_e\lambda^2)$, where r_e is the classical electron radius. The analysis results are summarized in Table 1. Similar XR data were obtained for a thinner C-PNME film (thickness 22.3 nm) [Fig. 5(a)]. However, in the XR profile for this film, the $\alpha_{c,f}$ is not easily discernible and the Kiessig fringes have a relatively low frequency, characteristics that can be attributed to the small film thickness. These XR data were also well fitted with the Parratt formalism using a structural model similar to that adopted in fitting

the XR data of the 140.6 nm-thick film. The results are listed in Table 1.

We also conducted similar analyses of the XR data of R-PNBE films with thicknesses of 21.1 and 125.0 nm. As shown in Fig. 5(b), the experimental data are well matched with the fitted curve. The analysis results are summarized in Table 1.

All the films annealed at 473 K were found to have a very thin skin layer whose electron density is slightly lower or higher than that of the bulk; the thickness of this skin layer ranged from 0.8 to 1.9 nm (Table 1). The surface roughnesses of the films were all around 0.1 nm, indicating that the films had very smooth surfaces. A similar skin layer and very low surface roughness were observed for other films of both types of polymer (data not shown). For both C-PNME and R-PNBE, the film electron density is greater for the thick film than for the very thin film. For films of similar thickness, the electron density is greater for the C-PNME film than for the R-PNBE film. These trends in film properties were observed both before and after annealing at 323 K (data not shown). Collectively, these electron density data indicate two important features of the molecular chain packing in the films: (1) in the film state, the C-PNME polymer chains tend to pack more densely than the R-PNBE polymer chains; and (2) for both polymers, the molecular chain packing density is higher in thick films (125.0 and 140.6 nm thick) than in very thin films (21.1 and 22.3 nm thick).

Taking into account the structural details obtained from the GIXS and XR analyses, the polymer films were further investigated by spectroscopic ellipsometry in order to investigate their optical and thermal expansion properties.

Fig. 6(a) shows the refractive indices (n_f) of the C-PNME films with various thicknesses measured before and after annealing at 423 K and 473 K. Both before and after thermal annealing, the n_f value of the C-PNME films increases slightly with decreasing thickness over the film thickness range of 60–467 nm, but decreases steeply with further decreases of the thickness below 60 nm. A similar trend is observed for the R-PNBE film, but the significant drop in refractive index occurs when the film thickness is decreased below 30 nm [Fig. 6(b)].

For a given polymer film, efficient molecular packing with appropriate chain orientation leads to a high electron density, which in turn results in a high refractive index. Taking this into consideration, along with the GIXS and XR results discussed above, the observation that n_f increases with decreasing film thickness for C-PNME and R-PNBE films with thicknesses of >60 nm and >30 nm, respectively, indicates that the overall molecular packing of the polymer chains in these films is enhanced as the film thickness is reduced. This enhancement of the polymer chain packing may be due to a combination of the in-plane chain orientation being favored in thinner films, as shown in the GIXS analysis discussed above, and in-plane oriented polymer chains having a better packing tendency.

In fact, the tendency toward enhanced in-plane chain orientation in a film increases both with decreasing film thickness as well as increasing polymer chain rigidity (Pyo *et al.*, 1999; Ree *et al.*, 1992; Ree *et al.*, 1994; Ree *et al.*, 1997). These trends would lead one to expect much larger n_f values for the C-PNME films of thickness <60 nm than for the R-PNBE films of thickness <30 nm; however, the opposite was observed in our results. This discrepancy can be attributed to the effect on the chain packing of the highly confined geometry of a very thin film supported on a substrate. In a substrate-supported thin film whose thickness is lower than a certain critical thickness, a high degree of in-plane chain orientation is always achieved, but the packing efficiency of the resulting in-plane oriented polymer chains is drastically reduced by the small number of polymer

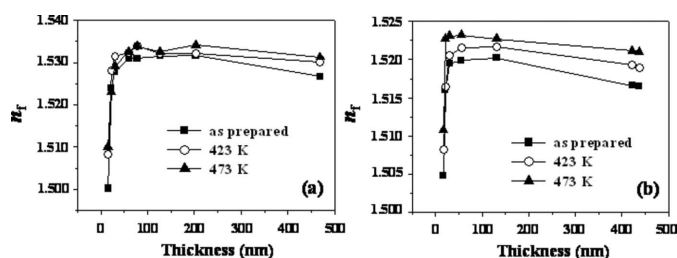


Figure 6

Variation of refractive index n_f (at $\lambda = 633$ nm) as a function of film thickness for (a) C-PNME and (b) R-PNBE films before and after annealing at 423 and 473 K.

chains in the system as well as restrictions on the chain mobility due to the interfaces of the film. These characteristics lead to loose chain packing in the film. In thick films, by contrast, chain packing can occur in both the out-of-plane and in-plane directions. These factors make it clear that dense molecular chain packing in a polymer film supported on a substrate can only occur if the system contains sufficient chains and if those chains are sufficiently mobile. Therefore, the significant n_f decreases observed in the *C*-PNME and *R*-PNBE films with thicknesses of <60 nm and <30 nm, respectively, are attributed to the restricted packing efficiency of polymer chains caused by the ultra-thin film confinement.

For all of the films, the film annealed at higher temperature has a higher n_f value, indicating that the thermal annealing process enhances the packing density of the polymer chains in the film.

For polymer films with the same or similar thicknesses prepared using the same process, the n_f value is always higher for the *C*-PNME film than for the *R*-PNBE film (Fig. 6). This result indicates that the *C*-PNME film has a higher molecular packing density and larger electron density, compared to those of the corresponding *R*-PNBE film, which is consistent with the findings of the XR analysis.

Fig. 7(a) shows the out-of-plane birefringence, $\Delta_{\perp} (= n_{xy} - n_z)$, as a function of annealing temperature for the films that were used in the GIXS analysis (Fig. 2). The measured Δ_{\perp} values are positive, regardless of the polymer type and annealing history. Taking into account that the films have some degree of in-plane chain orientation, as determined in the GIXS analysis, the positive Δ_{\perp} values indicate that both *C*-PNME and *R*-PNBE are positive birefringent polymers, which means that the polarization along the chain axis is greater than that along the direction normal to the chain axis. The as-prepared *C*-PNME film exhibits much larger Δ_{\perp} values than the as-prepared *R*-PNBE film, indicating that the *C*-PNME polymer chains are more linear and oriented in the film plane to a greater extent, compared to the *R*-PNBE polymer chains. This result supports the findings of the GIXS analyses and molecular simulations discussed above.

The Δ_{\perp} value of the *C*-PNME film is decreased by half after annealing at 423 K or 473 K. This observation indicates that annealing diminishes the in-plane orientation of the *C*-PNME polymer chains in the film, although a certain level of in-plane chain orientation is retained after thermal annealing at temperatures up to 473 K. In contrast, the out-of-plane birefringence of the *R*-PNBE film, which was very weak in the as-prepared film, decreases to almost zero after thermal annealing at 473 K, indicating that the *R*-PNBE film is formed with a weak out-of-plane optical anisotropy (*i.e.* a small degree of in-plane chain orientation) and that this weak optical

anisotropy is almost completely eliminated by thermal annealing. These results further indicate that the *R*-PNBE chain is much more flexible than the *C*-PNME chain.

We additionally performed ellipsometry measurements on the polymer films with various thicknesses during a heating run in which the sample temperature was raised from 303–323 K in increments of 5 K, with a heating rate of 3.0 K min⁻¹ for each step and a soaking time of 5 min at each temperature. From these measurements, we determined the out-of-plane thermal expansion coefficients (ε_{\perp}) of the films. Fig. 7(b) shows representative ε_{\perp} results obtained from films annealed at 473 K. As can be seen in the figure, the ε_{\perp} of the *C*-PNME film decreases slightly with decreasing thickness over the film thickness range of 140–500 nm but turns to steeply increase with further decreases of the thickness over the thickness range of <140 nm. Similarly, the ε_{\perp} value for the *R*-PNBE film also decreases very slowly with decreasing thickness over the range of 85–400 nm and turns to rapidly increase with further decreases of the thickness in the range of <85 nm [Fig. 7(b)]. Overall, the ε_{\perp} values are lower for the *C*-PNME film than for the *R*-PNBE film with a similar thickness. Taking into account the GIXS and XR results and the refractive index data, the observed ε_{\perp} variations can be attributed to the structural characteristics of the films, which depend on the film thickness. In particular, the ε_{\perp} results again confirm that the polymer chains are more loosely packed along the out-of-plane direction in the thinner films, revealing higher thermal expansion across the film thickness.

4. Conclusions

Two novel polynorbornenes, *C*-PNME and *R*-PNBE, prepared as substrate-supported thin films with various thicknesses, were investigated in detail using GIXS, XR and ellipsometry analyses. These analyses provided important information on the structural characteristics and properties of the polymers in thin film form, which is critical to determining the suitability of these materials for applications such as microelectronics and flat-panel displays. Both of the polymers had helical conformations; however, compared to *R*-PNBE, *C*-PNME was more linear along the helical axis due to its tacticity (*i.e.* chirality), and hence exhibited more rigid chain characteristics. The linear and rigid nature of the *C*-PNME polymer chains caused them to pack more densely and align more in the film plane. As a result, the *C*-PNME films exhibited higher refractive indices, higher optical anisotropy, and lower thermal expansion, compared to the *R*-PNBE films. In particular, it is noteworthy that the refractive indices of all of the films, which provide a measure of the dielectric constant, were much lower than those of the current workhorse dielectrics such as silicon oxide, silicon nitride, and polyimides. For both polymers, the film structural characteristics and properties were found to further depend on the film thickness and thermal annealing history. All of the films were found to have a very thin skin layer and very smooth surfaces.

This study was supported by the Korea Science and Engineering Foundation (National Research Lab Program) and by the Korean Ministry of Education (Brain Korea 21 Program). The GIXS and XR measurements at the PAL were supported by MOST and POSCO.

References

- Angiolini, S., Avidano, M., Bracco, R., Barlocco, C., Young, N. D., Trainor, M. & Zhao, X. (2003). *SID 03 Dig.* **34**, 1325–1327.

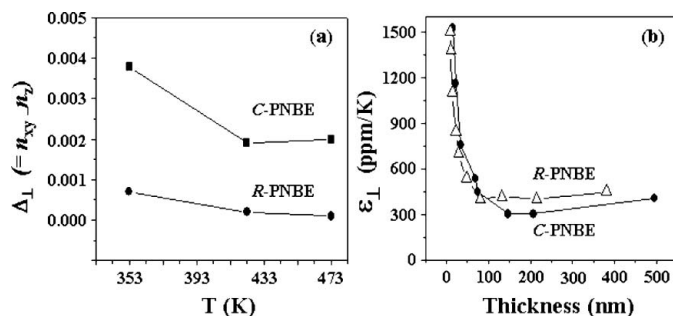


Figure 7
(a) Variation of the out-of-plane birefringence $\Delta_{\perp} (= n_{xy} - n_z)$ with annealing temperature T for 467 nm-thick *C*-PNME and 437 nm-thick *R*-PNBE films. n_{xy} and n_z are the in-plane and out-of-plane refractive indices of the film at $\lambda = 633$ nm, respectively. (b) Variation of the out-of-plane thermal expansion coefficient (ε_{\perp}) as a function of film thickness for *C*-PNME and *R*-PNBE films annealed at 473 K.

- Bhusari, D., Reed, H. A., Wedlake, M., Padovani, A. M., Bidstrup-Allen, S. A. & Kohl, P. A. (2001). *J. Microelectromech. Syst.* **10**, 400–408.
- Bolze, J., Kim, J., Huang, J.-Y., Rah, S., Youn, H. S., Lee, B., Shin, T. J. & Ree, M. (2002). *Macromol. Res.* **10**, 2–12.
- Bolze, J., Ree, M., Youn, H. S., Chu, S.-H. & Char, K. (2001). *Langmuir*, **17**, 6683–6691.
- Breunig, S. & Risse, W. (1992). *Makromol. Chem.* **193**, 2915–2927.
- Byun, G., Kim, S. Y. & Cho, I. (2006). *J. Polym. Sci. Part A Polym. Chem.* **44**, 1263–1270.
- Grove, N., Kohl, P. A., Bidstrup-Allen, S. A., Jayaraman, S. & Shick, R. (1999). *J. Polym. Sci. Part B Polym. Phys.* **37**, 3003–3010.
- Heinz, B. S., Alt, F. P. & Heitz, W. (1998). *Macromol. Rapid Commun.* **19**, 251–256.
- Kiessig, H. (1931). *Ann. Phys.* **10**, 769–788.
- Lipian, J., Mimna, R. A., Fondran, J. C., Yandulov, D., Shick, R. A., Goodall, B. L., Rhodes, L. F. & Huffman, J. C. (2002). *Macromolecules*, **35**, 8969–8977.
- Mathew, J. P., Reinmuth, A., Melia, J., Swords, N. & Risse, W. (1996). *Macromolecules*, **29**, 2755–2763.
- Park, B.-J., Rah, S.-Y., Park, Y.-J. & Lee, K.-B. (1995). *Rev. Sci. Instrum.* **66**, 1722–1724.
- Parratt, L. G. (1954). *Phys. Rev.* **95**, 359–369.
- Oh, W. & Ree, M. (2004). *Langmuir*, **20**, 6932–6939.
- Pyo, S. M., Kim, S. I., Shin, T. J., Park, Y. H. & Ree, M. (1999). *J. Polym. Sci. Part A Polym. Chem.* **37**, 937–957.
- Ree, M., Chen, K. J., Kirby, D. P., Katzenellenbogen, N. & Grischkowsky, D. (1992). *J. Appl. Phys.* **72**, 2014–2021.
- Ree, M., Chu, C. W. & Goldberg, M. J. (1994). *J. Appl. Phys.* **75**, 1410–1419.
- Ree, M., Kim, K., Woo, S. H. & Chang, H. (1997). *J. Appl. Phys.* **81**, 698–708.
- Ree, M. & Ko, I. S. (2005). *Phys. High Tech. (Korea)*, **14**, 2–7.
- Reinmuth, A., Mathew, J. P., Melia, J., Risse, W. (1996). *Macromol. Rapid Commun.* **17**, 173–180.
- Shick, R. A., Jayaraman, S. K., Goodall, B. L., Rhodes, L. F., McDougall, W. C., Kohl, P. A., Bidstrup-Allen, S. A. & Chiniwalla, P. (1998). *Adv. Microelectron.* **25**, 13–14.
- Shin, B., Jang, M., Yoon, D. Y. & Heitz, W. (2004). *Macromol. Rapid Commun.* **25**, 728–732.
- Yu, C.-J., Kim, J., Kim, K.-W., Kim, G.-H., Lee, H.-S., Ree, M. & Kim, K.-J. (2005). *J. Kor. Vac. Soc.* **14**, 138–142.